

SUPPORTING INFORMATION

Supporting Information

Electronic supplementary information (ESI)

Ultra-Fast and Stable Extraction Li metal from Seawater

Xuemei Zhao, Haiquan Zhang*, Yihui Yuan, Yuxi Ren, and Ning Wang*

State Key Laboratory of Marine Resource Utilization in South China Sea, Hainan University, Haikuo 570228, P. R. China
E-mail: wangn02@foxmail.com

Experimental Procedures

Materials and Methods

The LLAZO powder was synthesized via the spark plasma sintering (SPS) technique. The starting materials were Li_2CO_3 (99%, Aladdin), $\text{La}(\text{NO}_3)_3$ (99.9%, Aladdin), $\text{ZrO}(\text{NO}_3)_2$ (99.9%, Aladdin), and Al_2O_3 (99.99%, Aladdin). Stoichiometric amounts of these chemicals were dispersed in deionized water and a 10% excess of Li_2CO_3 was added to compensate for Li volatilization during the high-temperature pellet preparation. The ball-milled mixture was evaporated at 393 K for 12 hours and then calcined to 1173 K for 12 hours to synthesize the precursor powder. The powders were then pressed into pellets, which were sintered at 673-1173 K for 10 min by the spark plasma sintering (SPS) technique. The LLAZO pellets (≥ 3 mm) were then sintered at 1423-1523 K for 24 h with more of the LLAZO powder covering them in order to improve their crystallinity. The sintered LLAZO pellets were polished to ~ 500 μm thickness with a smooth surface.

Material characterization

Scanning electron microscopy (SEM) was performed with a Hitachi S-4800 analytical scanning electron microscope. The element distribution of the garnet SSE pellet was tested by Energy-dispersive spectroscopy mapping (EDS). The crystal phase analysis was performed by powder X-ray diffraction with a D8 ADVANCE with LynxEye and SolX (Bruker AXS) using a $\text{Cu K}\alpha$ radiation source operated at 40 kV and 40 mA. Inductively coupled plasma mass spectrometry (ICP-MS) was used to measure the amount of Li metal deposited

on the cathode. The contact angle between seawater and the garnet LLAZO solid-stated electrolyte were determined using a contact angle meter.

Relative density characterization

The density of the sintered pellets was performed in water by the Archimedes method. Fresh LLZO garnet pellet is dried at 100 °C for 12 h, and its mass is M_1 ; their apparent and true volumes are equal to V_0 and V^* , respectively. The garnet is immersed in water for 30 min. The pellet is hung in the water and weighed, and recorded as M_2 ; the garnet is removed from the water, and the excess water on the surface is wiped off. The mass is M_3 . The density of water is recorded as ρ_0 .

$$\text{Relative density } (\eta): \eta = \frac{M_1/V_0}{M_1/V^*} = \frac{(M_1 - M_2)/\rho_0}{(M_3 - M_1)/\rho_0 + (M_1 - M_2)/\rho_0} = \frac{M_1 - M_2}{M_3 - M_2}$$

Electrochemical characterization

The garnet LLAZO pellet was wet-polished using sandpaper and rinsed with ethanol several times. The thickness (~500 μm) of the garnet ceramic was controlled. To measure the ionic conductivity of the garnet SSE, both sides of the ceramic pellet were coated with an Au layer, which served as a blocking electrode. Electrochemical impedance spectroscopy (EIS) was performed across a frequency range of 1 MHz to 100 mHz with a 50 mV perturbation amplitude. Conductivities were calculated using $\sigma = h/(Z \times A)$, where Z is the impedance for the real axis in the Nyquist plot, h is the garnet ceramic disc length, and A is the surface area. The Li extraction devices were assembled in an Ar filled glove-box using fresh Cu foil ($A = 3.14 \text{ cm}^2$) and garnet $\text{Li}_{6.75}\text{La}_3\text{Al}_{0.25}\text{Zr}_2\text{O}_{12}$ pellet ($h = 500 \text{ }\mu\text{m}$; $A = 7.065 \text{ cm}^2$) as the inert cathode and solid-state electrolyte, respectively. And the liquid organic electrolyte was

1 M LiPF_6 dissolved in a mixture of ethylene carbonate (EC) and dimethyl carbonate (DMC) (1:1 by volume). The SSE pellet, Cu electrode and liquid organic electrolyte are sequentially placed in a self-made mold in Figure S5. The lithium extraction device is sealed with paraffin to prevent the liquid organic electrolyte from coming into contact with the air. The packaged device was placed in natural seawater and was combined with an inert Pt electrode ($A = 3.14 \text{ cm}^2$) to form a complete electrolytic cell. The contact area of LLAZO SSE with seawater is 0.785 cm^2 . In order to ensure that the concentration of Li-ions remained unchanged, 1 ton of flowing natural seawater was used for lithium extraction experiments in seawater. Electrochemical performances, such as constant current charge/discharge curves, cyclic voltammogram, linear sweep voltammetry and AC electrochemical impedance spectroscopy, were carried out using electrochemical workstation (Shanghai Chenhua Instrument Co., Ltd., CHI660e). Seawater collected from the South China Sea near the Boundary Island was filtered through a $0.22 \text{ }\mu\text{m}$ filter to remove insoluble particles and microorganisms.)

Data analysis

Table

Table 1 Summary of Li-ion solid-state electrolyte materials.

Li-ion solid-state electrolyte		Ionic conductivity [S cm ⁻¹]	Voltage window [V]	Stability to H ₂ O	Stability to Li	Reference
Sulfide	Li ₃ PS ₄	2×10 ⁻⁷	-	Poor	Poor	[1]
	Li _{3.25} Ge _{0.25} P _{0.7} S ₄	2×10 ⁻³	-	Poor	Poor	[2]
Hydride	LiAlH ₄	2×10 ⁻⁹	-	Poor	Good	[3]
	Li ₂ NH	2×10 ⁻⁴	-	Poor	Good	[4]
Halide	Li ₂ CdI ₄	1×10 ⁻⁹	7	Poor	Good	[5]
	Li ₂ CdCl ₄	1×10 ⁻⁶	7	Poor	Good	[6]
Nitride	Li ₇ PN ₄	1×10 ⁻⁷	-	Poor	Good	[7]
	Li ₃ N	1×10 ⁻³	0.44	Poor	Good	[8]
Perovskite	Li _{0.34} Nd _{0.55} TiO ₃	3×10 ⁻⁸	-	Good	Poor	[9]
	Li _{0.34} La _{0.51} TiO _{2.94}	1×10 ⁻⁴	-	Good	Poor	[10]
NASICON	LiGe ₂ (PO ₄) ₃	3×10 ⁻⁶	-	Good	Poor	[11]
	Li _{1.3} Al _{0.3} Ti _{1.7} (PO ₄) ₃	3×10 ⁻³	-	Good	Poor	[12]
Thin film	LiPON	1×10 ⁻⁶	5	Poor	Good	[13]
Polymer	PEO	1×10 ⁻⁴	≤ 4	Poor	Good	[14]
Garnet	Li ₇ La ₃ Zr ₂ O ₁₂	2×10 ⁻⁶	6	Good	Good	[15,16]
	Li _{7-x} La ₃ Al _x Zr ₂ O ₁₂	2×10 ⁻⁴	6	Good	Good	[17]

NASICON, sodium superionic conductor; LiPON, lithium phosphorous oxynitride; PEO, poly(ethylene oxide).

Although a large number of Li-ion SSEs have been reported (Table 1), the materials available for electrochemical extraction device are extremely limited. Sulfide-type materials^[1,2], such as Li₁₀GeP₂S₁₂ (LGPS), have a high ionic conductivity (0.01 S cm⁻¹) but are unstable toward Li metal. These compounds rapidly decompose forming Li₃P, Li₂S and Ge. Li-nitride/-hydride/-halide^[3,8] have a good stability with Li metal. However, the chemical stability of these SSE materials is poor, and the materials are sensitive to moisture. The representative Perovskite solid-state electrolyte is Li_{3x}La_{2/3-x}TiO₃, which exhibits a Li-ion conductivity exceeding 10⁻³ S cm⁻¹ at room temperature.^[9,10] Unfortunately, it has been deemed unsuitable in Li metal extraction

device because of the reduction Ti^{4+} on contact with Li metal production. $LiGe_2(PO_4)_3$ (LGP, NASICON) is known as a fast Li-ion conductor with a theory specific capacity of 540 mAh g^{-1} with formation of alloy $Li_{4.4}Ge$.^[11] $Li_{1.3}Al_{0.3}Ti_{1.7}(PO_4)_3$ ^[12] has the highest bulk conductivity ($3 \times 10^{-3} \text{ S cm}^{-1}$) for NASICON Li-ion conductors at room temperature. It is typically stable toward water and is stable at high potentials, but Ti^{4+} of compounds can be reduced with Li metal. LiPON materials, such as $Li_{3.3}PO_{3.9}N_{0.17}$ ^[13], display a relatively low ionic conductivity of $10^{-6} \text{ S cm}^{-1}$ and poor stability for air atmosphere. Composite polymer electrolytes^[14] consist of the polymer host (PEO, PAN, PMMA or PVDF) and $LiClO_4$ -organic solvents, which is inferior stability to air atmosphere.

A good alternative to these SSEs is the garnet-type oxides with general formula $A_3B_2C_3O_{12}$ where A-, B-, C- sites have dodecahedral (D_d), octahedral (O_h), and tetrahedral (T_d) coordinations, respectively. Garnet $Li_7La_3Zr_2O_{12}$ (LLZO)^[15-17] is a promising solid-state electrolyte material for Li metal extraction device, as it features the advantages of low sintering temperature, stability toward Li metal and H_2O , and wide voltage window (0–6 V).

[1] S. Chen, J. Wang, Z. Zhang, L. Wu, L. Yao, Z. Wei, Y. Deng, D. Xie, X. Yao, X. Xu, *J. Power Sources* **2018**, *387*, 72-80.

[2] K. Suzuki, D. Kato, K. Hara, T. –A. Yano, M. Hirayama, M. Hara, R. Kanno, *Electrochim. Acta* **2017**, *258*, 110-115.

[3] H. Oguchi, M. Matsuo, T. Sato, H. Takamura, H. Maekawa, H. Kuwano, S. Orimo, *J. Appl. Phys.* **2010**, *107*, 096104.

[4] Y. Zhang, L. Zhan, X. Zhuang, Y. Zhu, N. Wan, X. Guo, J. Chen, Z. Wang, L. Li, *J. Alloy. Compd.* **2017**, *695*, 2894-2901.

- [5] J. C. Bachman, S. Muy, A. Grimaud, H. -H. Chang, N. Pour, S. F. Lux, O. Paschos, F. Maglia, S. Lupart, P. Lamp, L. Giordano, Y. Shao-horn, *Chem. Rev.* **2015**, *116*, 140-162.
- [6] H. D. Lutz, W. Schmidt, H. Haeuseler, *J. Phys. Chem. Solids* **1981**, *42*, 287-289.
- [7] A. Al-Qawasmeh, N. A. W. Holzwarth, *J. Power Sources* **2017**, *364*, 410-419.
- [8] K. Park, J. B. Goodenough, *Adv. Energy Mater.* **2017**, *7*, 1700732.
- [9] M. Itoh, Y. Inaguma, W. -H. Jung, L. Chen, T. Nakamura, *Solid State Ionics* **1994**, *70-71*, 203-207.
- [10] Z. Zheng, H. Fang, Z. Liu, Y. Wang, *J. Electrochem. Soc.* **2015**, *162*, A244-A248.
- [11] J. Feng, H. Xia, M. O. Lai, L. Lu, *J. Phys. Chem. C* **2009**, *113*, 20514-20520.
- [12] M. Monchak, T. Hupfer, A. Senyshyn, H. Boysen, D. Chernyshov, T. Hansen, K. G. Schell, E. C. Bucharsky, M. J. Hoffmann, *H. Ehrenberg, Inorg. Chem.* **2016**, *55*, 2941-2945.
- [13] Y. Zhu, X. He, Y. Mo, *Adv. Sci.* **2017**, *4*, 1600517.
- [14] C. Wang, Y. Yang, X. Liu, H. Zhong, H. Xu, Z. Xu, H. Shao, F. Ding, *ACS Appl. Mater. Inter.* **2017**, *9*, 13694-13702.
- [15] F. Han, Y. Zhu, X. He, Y. Mo, C. Wang, *Adv. Energy Mater.* **2016**, *6*, 1501590.
- [16] E. Kazyak, K. H. Chen, K. N. Wood, A. L. Davis, T. Thompson, A. R. Bielinski, A. J. Sanchez, X. Wang, C. Wang, J. Sakamoto, N. P. Dasgupta, *Chem. Mater.* **2017**, *29*, 3785-3792.
- [17] N. Rosenkiewitz, J. Schuhmacher, M. Bockmeyer, J. Deubener, *J. Power Sources* **2015**, *278*, 104-108.

Table 2 Summary of Li-ion solid-state electrolyte materials.

Methods	Materials	Li-ion concentration ppm	i mA cm ⁻²	M mg g ⁻¹	t h	S m ² g ⁻¹	μ μg cm ⁻² h ⁻¹	Reference
Adsorption	MnO ₂ ion sieve	17		62	120	-	0.0052	18
	MnO ₂ ion sieve	6		10	48	-	0.0021	19
	PVC-MnO ₂ ion sieve	224		20	72	34	0.0008	20
	PAM-MnO ₂ ion sieve	137		18.2	48	-	0.0038	21
	H ₂ TiO ₃	1000		59.1	12	16	0.0308	22
	H ₂ TiO ₃	70		28.7	24	17.9	0.0067	23
	H ₂ TiO ₃	87.5		28.6	50	-	0.0057	24
	PVA/H ₂ TiO ₃	7		13.5	24	10	0.0056	25
Electrolysis	Li _{1+x} Al _y Ge _{2-y} (PO ₄) ₃	0.2	0.24				57	26
	Li _{6.75} La ₃ Al _{0.25} Zr ₂ O ₁₂	0.2	0.76				198	Our work

[18] S. Zandevakili, M. Ranjbar, M. Ehteshamzadeh, *Hydrometallurgy*, 2014, **149**, 148.

[19] L. F. Liu, H. W. Zhang, Y. S. Zhang, D. M. Cao, X. H. Zhao, *Colloid. Surface. A*, 2015, **468**, 280.

[20] G. P. Xiao, K. F. Tong, L. S. Zhou, J. L. Xiao, S. Y. Sun, P. Li, J. G. Yu, *Ind. Eng. Chem. Res.*, 2012, **51**, 10921.

[21] J.-L. Xiao, S.-Y. Sun, X. Song, P. Li, J.-G. Yu, *Chem. Eng. J.* 2015, **279**, 659.

[22] S. D. Wei, Y. F. Wei, T. Chen, C. B. Liu, Y. H. Tang, *Chem. Eng. J.* 2020, **379**, 122407.

[23] C. P. Lawagon, G. M. Nisola, J. Mun, A. Tron, R. E. C. Torrejos, J. G. Seo, H. Kim, W. – J. Chung, *J. Ind. Eng. Chem.*, 2016, **35**, 347.

[24] X. –C. Shi, Z. –B. Zhang, D. F. Zhou, L. –F. Zhang, B. –Z. Chen, L. –L. Yu, *T. Nonferr. Metal. Soc.*, 2013, **23**, 253.

[25] L. Y. Zhang, D. L. Zhou, G. He, F. H. Wang, J. B. Zhou, *Mater. Lett.*, 2014, **135**, 206.

[26] S. Yang, F. Zhang, H. Ding, P. He, H. Zhou, *Joule*, 2018, **2**, 1648.

Figure

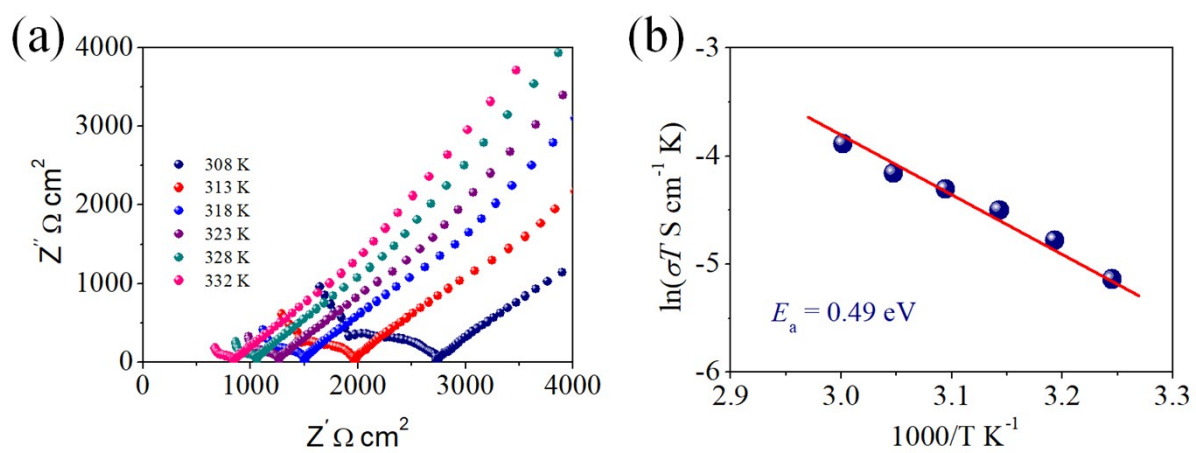


Figure S1. Characterization of the garnet $\text{Li}_7\text{La}_3\text{Zr}_2\text{O}_{12}$ solid-state electrolyte. (a) EIS; (b) Arrhenius plot.

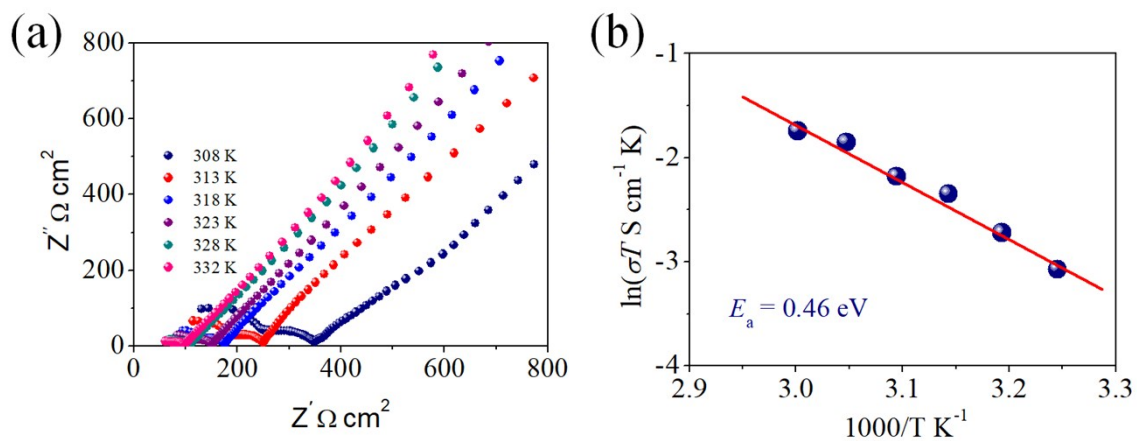


Figure S2. Characterization of the Li_{6.75}La₃Al_{0.25}Zr₂O₁₂. (a) EIS; (b) Arrhenius plot.

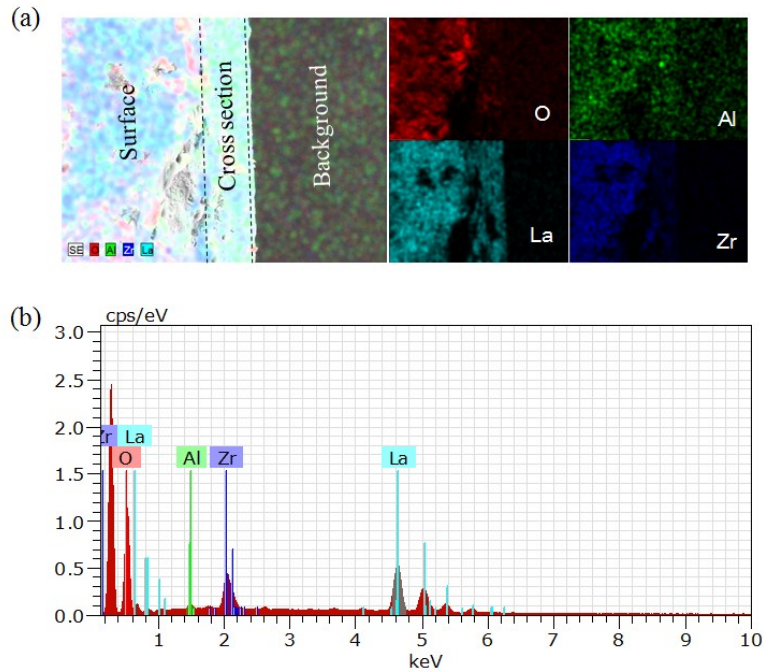


Figure S3. EDS-Mapping (a) and EDS (b) of the LLAZO SSE.

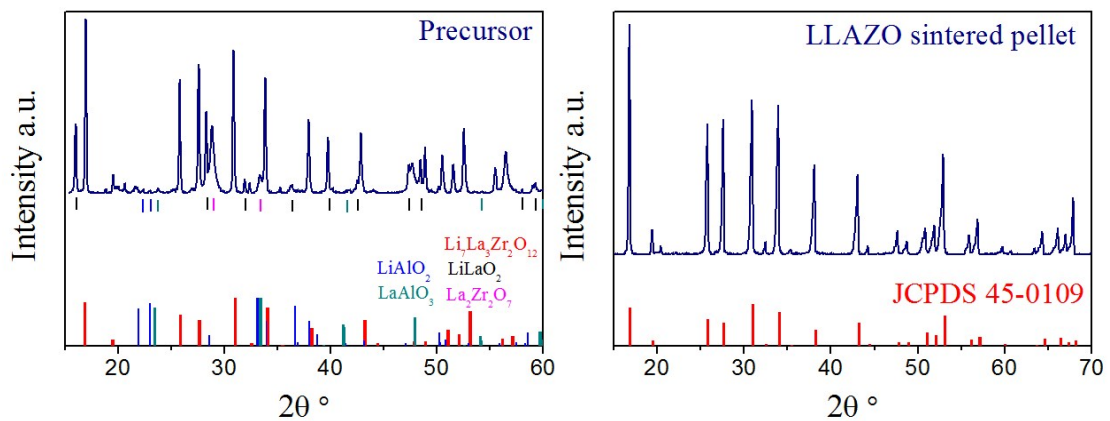


Figure S4. XRD pattern of the precursor powder and $\text{Li}_{6.75}\text{La}_3\text{Al}_{0.25}\text{Zr}_2\text{O}_{12}$ SSE.

Figure S4 displays XRD pattern of the precursor powder and $\text{Li}_{6.75}\text{La}_3\text{Al}_{0.25}\text{Zr}_2\text{O}_{12}$ ceramic pellet. The diffraction peaks of LiAlO_2 and LaAlO_2 are observed in the white precursor

powder. However, only cubic garnet phase is detected in the ultra-dense LLAZO SSE, which is consistent with the results reported in the literatures²⁷⁻³¹. Therefore, Al does participate in the formation of LLZO's crystal structure, rather than in a mixed form. In contrast, a significant tetragonal splitting is observed for the un-stabilized $\text{Li}_7\text{La}_3\text{Zr}_2\text{O}_{12}$, as evidenced by the enlarged local (213) and (426) diffraction lines.^{32,33} This proves that Al can strengthen the crystal structure of cubic garnet.

[27] T. Thompson, J. Wolfenstine, J. L. Allen, *J. Mater. Chem. A*, 2014, **2**, 13431.

[28] N. Rosenkiewitz, J. Schuhmacher, M. Bockmeyer, *J. Power Sources*, 2015, **278**, 104.

[29] S. H. Yang, M. Y. Kim, D. H. Kim, *J. Ind. Eng. Chem.*, 2017, **56**, 422.

[30] A. N. Wang, J. F. Nonemacher, G. Yan, *J. Eur. Ceram. Soc.*, 2018, **38**, 3201.

[31] Y. Li, Y. Cao, X. Guo, *Solid State Ion.*, 2013, **253**, 76.

[32] X. P. Wang, Y. X. Gao, Y. P. Xia, *Phys. Chem. Chem. Phys.*, 2014, **16**, 7006.

[33] M. A. Howard, O. Clemens, E. Kendrick, *Dalton Trans.*, 2012, **41**, 12048.

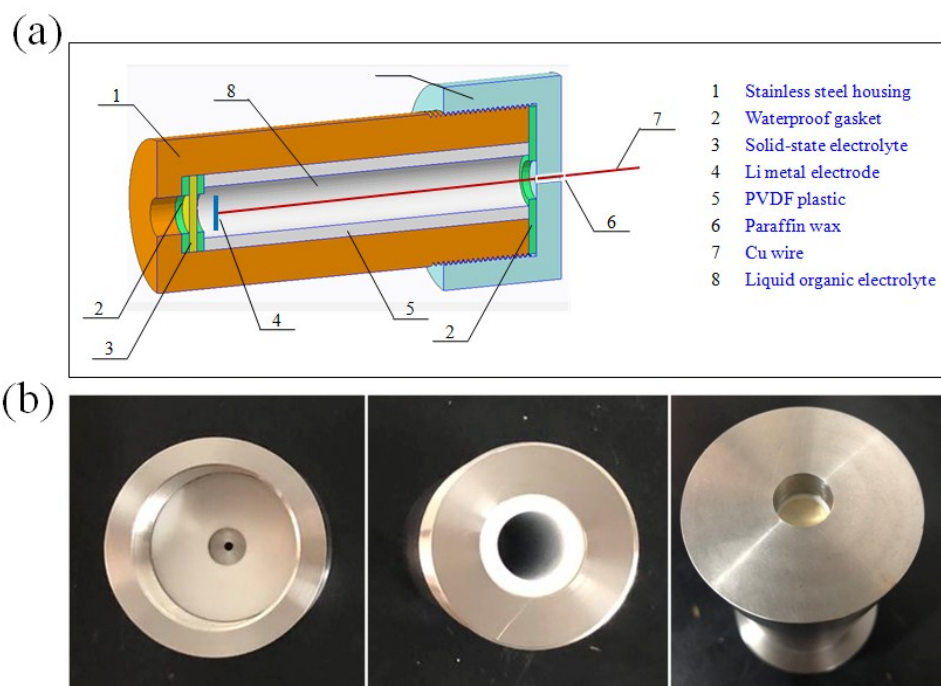


Figure S5. Structure of self-made molds for extracting lithium from seawater. (a) Schematic diagram; (b) digital photos. **Note:** The Li extraction devices were assembled in an Ar filled glove-box using fresh Cu foil ($A = 3.14 \text{ cm}^2$) and garnet $\text{Li}_{6.75}\text{La}_3\text{Al}_{0.25}\text{Zr}_2\text{O}_{12}$ pellet ($h = 500 \text{ }\mu\text{m}$; $A = 7.065 \text{ cm}^2$) as the inert cathode and solid-state electrolyte, respectively. And the liquid organic electrolyte was 1 M LiPF_6 dissolved in a mixture of ethylene carbonate (EC) and dimethyl carbonate (DMC) (1:1 by volume). The SSE pellet, Cu electrode and liquid organic electrolyte are sequentially placed in a self-made mold in Figure S5. The lithium extraction device is sealed with paraffin to prevent the liquid organic electrolyte from coming into contact with the air. The packaged device was placed in natural seawater and was combined with an inert Pt electrode ($A = 3.14 \text{ cm}^2$) to form a complete electrolytic cell. The contact area of LLAZO SSE with seawater is 0.785 cm^2 . In order to ensure that the concentration of Li-ions remained unchanged, 1 ton of flowing natural seawater was used for lithium extraction experiments in seawater.

Charge

Cathode: $Li^+(aq) + e^- \rightarrow Li(s)$
Anode: $2H_2O(l) \rightarrow O_2(g) + 4H^+(aq) + 4e^-$
Nernst equation: $\varphi = \varphi^\ominus - \frac{RT}{zF} \ln \prod_B (a_B)^{\nu_B}$

$$\varphi_{Li^+} = \varphi_{Li^+}^\ominus - \frac{RT}{zF} \ln \left(\frac{a\{Li(s)\}}{a\{Li^+\}} \right) = 3.04V$$

$$\varphi_{OH^-} = \varphi_{OH^-}^\ominus - \frac{RT}{zF} \ln \frac{a^4\{H^+\} p\{O_2(g)\} / p^\ominus\{O_2(g)\}}{a^2\{H_2O\}}$$

$$= \varphi_{OH^-}^\ominus - \frac{RT}{F} \ln a\{H^+\}$$

$$= -1.23 + 0.41$$

$$= -0.82V$$

$$\Delta\varphi_1^* = \varphi_{Li^+} - \varphi_{OH^-} = 3.86V$$

Discharge

Cathode: $2H_2O(l) + O_2(g) + 4e^- \rightarrow 4OH^-(aq)$
Anode: $Li(s) \rightarrow Li^+(aq) + e^-$
Nernst equation: $\varphi = \varphi^\ominus - \frac{RT}{zF} \ln \prod_B (a_B)^{\nu_B}$

$$\varphi_{Li^+} = \varphi_{Li^+}^\ominus - \frac{RT}{zF} \ln \left(\frac{a\{Li^+\}}{a\{Li(s)\}} \right) = -3.04V$$

$$\varphi_{OH^-} = \varphi_{OH^-}^\ominus - \frac{RT}{zF} \ln \frac{a^4\{OH^-\}}{a^2\{H_2O\} p\{O_2(g)\} / p^\ominus\{O_2(g)\}}$$

$$= \varphi_{OH^-}^\ominus - \frac{RT}{F} \ln a\{OH^-\}$$

$$= 0.40 + 0.41$$

$$= 0.81V$$

$$\Delta\varphi_1^* = \varphi_{OH^-} - \varphi_{Li^+} = 3.86V$$

Cathode: $2H_2O(l) + 4e^- \rightarrow 2OH^-(aq) + H_2(g)$
Anode: $Li(s) \rightarrow Li^+(aq) + e^-$
Nernst equation: $\varphi = \varphi^\ominus - \frac{RT}{zF} \ln \prod_B (a_B)^{\nu_B}$

$$\varphi_{Li^+} = \varphi_{Li^+}^\ominus - \frac{RT}{zF} \ln \left(\frac{a\{Li^+\}}{a\{Li(s)\}} \right) = -3.04V$$

$$\varphi_{OH^-} = \varphi_{OH^-}^\ominus - \frac{RT}{zF} \ln \frac{a^2\{OH^-\} p\{H_2(g)\} / p^\ominus\{H_2(g)\}}{a^2\{H_2O\}}$$

$$= \varphi_{OH^-}^\ominus - \frac{RT}{F} \ln a\{OH^-\}$$

$$= -0.83 + 0.41$$

$$= -0.42V$$

$$\Delta\varphi_2^* = \varphi_{OH^-} - \varphi_{Li^+} = 2.62V$$

Figure S6. Calculation result of electrode potential based on the Nernst formula.

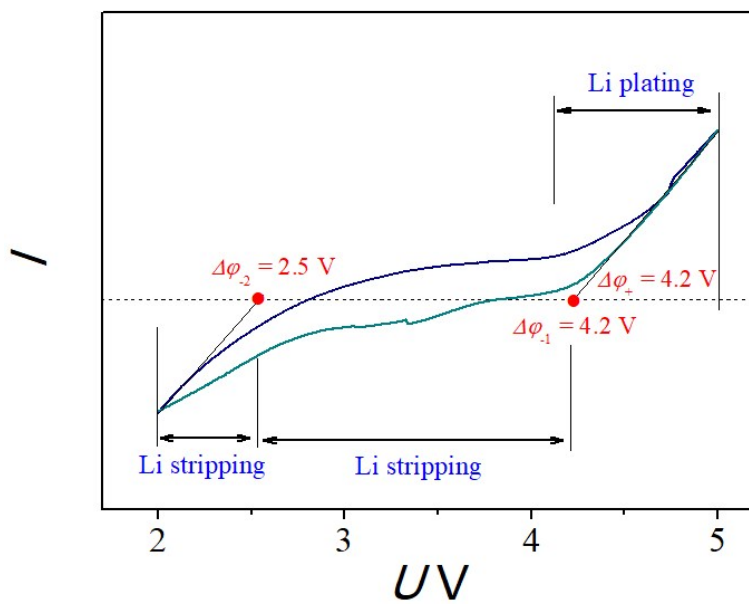


Figure S7. CV curve of the electrochemical device in seawater for Li extraction device.

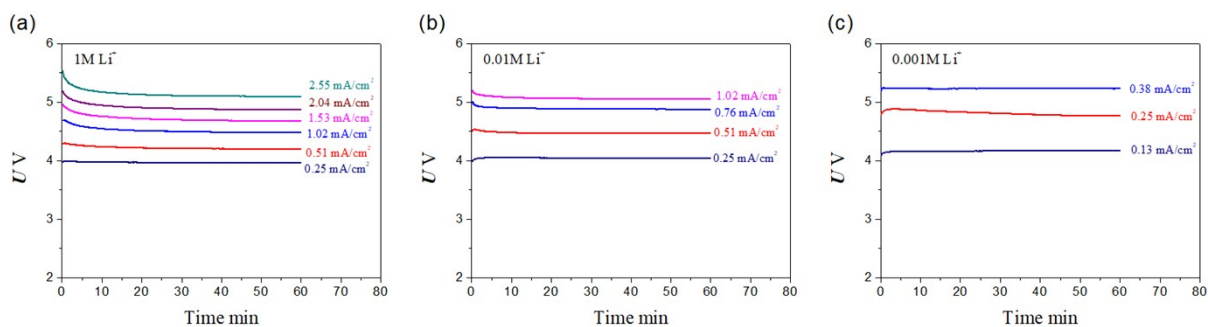


Figure S8. Potential-time profiles of the electrolysis process for 1 (a), 0.01 (b) and 0.001 (c) mol L^{-1} LiNO_3 solution.

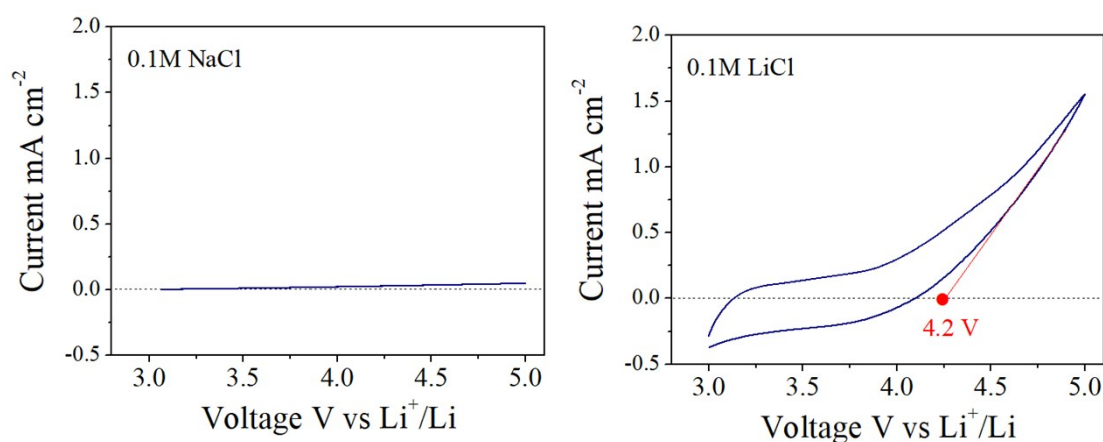


Figure S9. CV curves of the 0.1 M NaCl and LiCl solution for the electrochemical device.

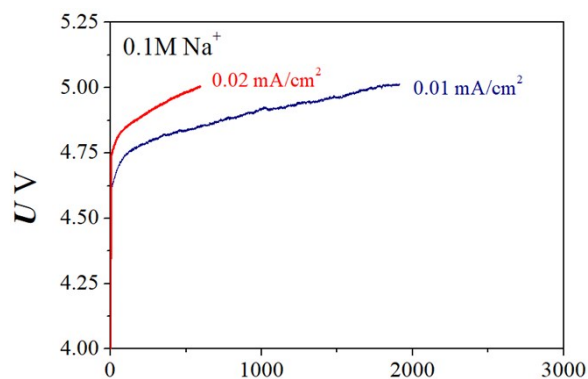


Figure S10. $U-t$ curves of the NaCl solution for the electrochemical device.

The main cation is Na^+ in seawater. We test the CV and $U-t$ curves of the 0.1 M NaCl and LiCl solution for the electrochemical device. It can be seen from Figure S9 that when the

solution is sodium chloride, the CV curve only detects the background current; for lithium chloride solution, the corresponding current is very obvious during the metal lithium deposition process. This shows that ultra-dense LLAZO allows only lithium ions to pass. For the constant current test results (Figure 5), the voltage-time curve cannot get a stable voltage plateau, even at a current density of 0.01 mA cm^{-2} . This also shows that the LLAZO solid-state electrolyte does not allow sodium ions to pass through the crystal.

In Li7-Garnet, most of Li^+ is located in the octahedral gap, and even a few are near the coplanar surface of the tetrahedron and octahedron. The large number of Li^+ and its Coulomb repulsion force the originally stable 24d position Li^+ to migrate, forming 96h \leftrightarrow 24d \leftrightarrow 96h migration path^{34,35}. Whether ions can be transported in the bulk phase is controlled by the ion radius and ion valence. The Li-ion is 76 pm, which is much smaller than the radius of equivalent ions (Na^+ , 102 pm; K^+ , 138 pm). This means that Na, K ions cannot be transported in the LLZO bulk phase. Although the ionic radius of Al is only 53.5 pm, its charge is much higher than that of Li-ion. The barrier to migration in tetrahedron is extremely high. It is impossible to transport in the bulk phase of LLZO, and it is also the theoretical basis for Al- or Ga-doped LLZO. On the other hand, inorganic materials such as lithium manganate and lithium titanate have been used in salt lake lithium extraction because they only selectively adsorb lithium ions.

[34] K. Hayamizu, S. Seki, T. Haishi, *J. Chem. Phys.*, 2017, **146**, 024701.

[35] K. Meier, T. Laino, A. Curioni, *J. Chem. Phys. C*, 2014, **118**, 6668.

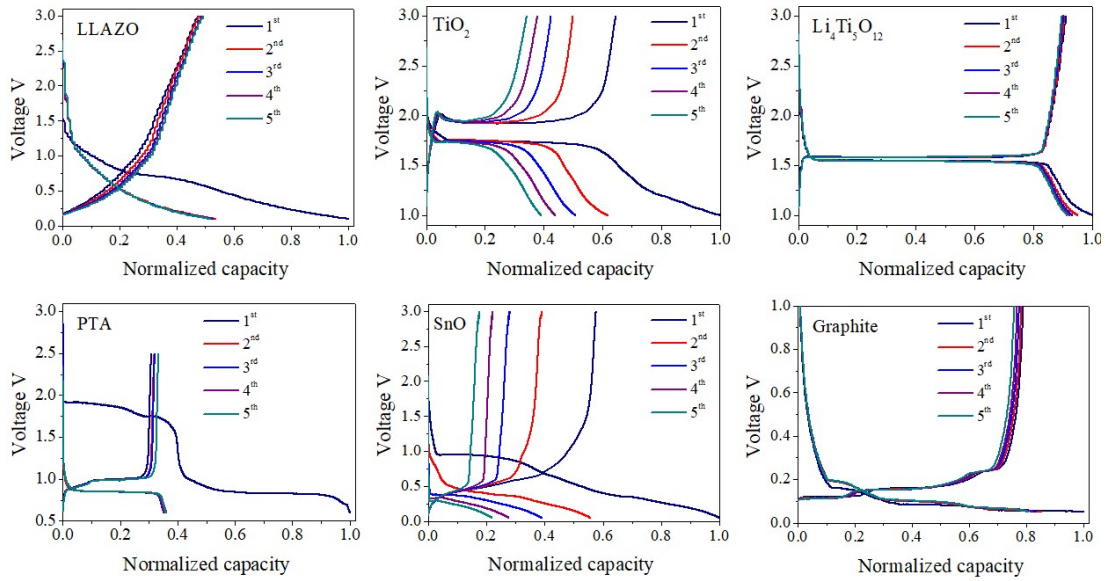


Figure S11. Constant current charge-discharge curves of LLZO, TiO_2 , $\text{Li}_4\text{Ti}_5\text{O}_{12}$, terephthalic acid (PTA), SnO and graphite.

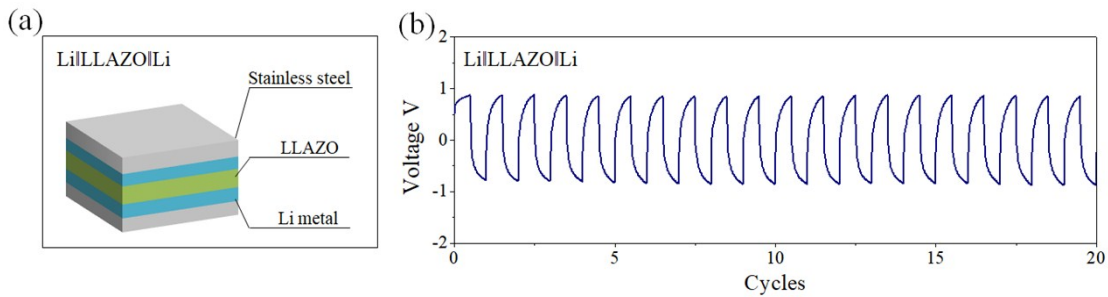


Figure S12. Diagram (a) and charge-discharge cycling performances (b).

Prove: ①stabilization of the cubic garnet phase, ②creation of vacancies in the C-site, and ③densification of the calcinations process.

① Stabilization of the cubic garnet phase :

Figure S4 presents the XRD pattern of the Al-stabilized. The Al-stabilized $\text{Li}_7\text{La}_3\text{Zr}_2\text{O}_{12}$ exhibits a typical garnet-type structure with cubic symmetry and no other impurity phases are found in the XRD pattern. In contrast, a significant tetragonal splitting is observed in the

un-stabilized $\text{Li}_7\text{La}_3\text{Zr}_2\text{O}_{12}$, as evidenced by the enlarged local (213) and (426) diffraction lines.

27-31

The electrochemical properties of the active materials are measured by assembling half cells. The LLAZO working electrode is prepared by casting N-methyl-2-pyrrolidone (NMP) slurry onto a Cu foil with the active material, carbon black as conducting additive and polyvinylidene fluoride (PVDF) as the binder at a weight ratio of 8:1:1. The CT2001A test cell is assembled in an Ar filled glove-box using Li metal foil and polypropylene (PP) membrane (Celgard 2400) as the counter electrode and the separator, respectively. The charge/discharge measurements were carried out under desired current densities with the voltage between 0.01 and 3.0 V. No stable discharge/charge platform voltage is observed on the constant current charge-discharge curve in Figure 6 (Figure 1b in supporting information), indicating that LLAZO is stable to metallic Li. For comparison, the electrochemical performance of TiO_2 , $\text{Li}_4\text{Ti}_5\text{O}_{12}$, terephthalic acid (PTA), SnO, and graphite are examined. Obvious voltage plateaus are observed at 1.7-2.0, 1.5-1.6, 0.8-1.0, 0.1-0.6, and 0.05-0.3 V in turn, indicating that they are active on metallic Li. Figure S11 shows that $\text{LiGe}_2(\text{PO}_4)_3$ is electrochemically active on metallic Li. This proves that LLAZO is stable to metallic lithium.

Assemble the all-solid-state lithium-ion battery according to the Figure S10a. It shows very good cycling performance in Figure S10b, showing that LLAZO is stable against metallic lithium.

② Increase in the average neck size

First-principles calculations can learn the form of elemental doping and the distribution probability of occupied positions^{36,37}. The actual distribution needs to be aided by neutron diffraction³⁸ or magic angle spinning (MAS) nuclear magnetic resonance (NMR)

spectroscopy³⁹. High-resolution X-ray diffraction (HRXRD)²⁷⁻³¹ can detect the effect of impurity elements on the unit cell parameters.

Based on *ab initio* calculations, Xu et al.⁴⁰ have proposed two potential pathways of Li-ion migration in the cubic garnets (route A and route B) with lithium contents 45 per formula unit. In route A, the Li-ion migrates *via* the interstice between neighboring octahedral sites, bypassing their common tetrahedral neighbor. In route B, the Li-ion moves through the shared triangular faces (“neck”) of the octahedral and tetrahedral sites. The Li-ion migration in route A is associated with an activation energy of 0.8 eV and is preferred when Li⁺ content is lower, such as Li₅La₃Nb₂O₁₂, while route B is associated with an activation energy of 0.26 eV and is preferred in highly Li-stuffed garnets such as Li₇La₃Zr₂O₁₂.⁴¹

Generally speaking, Al and Ga are doped at Li site; Ta and Nb are doped at Zr site; Ca, Sr, Ba and Ce are doped at La site. For Al doping, the order of site preference was Li (24d tetrahedral site) > Li (96h octahedral site) > Zr(16a) >> La (24c). For Al-doped compounds, the lattice expands with increased Al content filling the tetrahedral site. The site sizes do not significantly change with Al-doping, but the neck size expands. Even though Al³⁺ occupies the tetrahedral sites and is thought to be a “blocking” to Li conduction, its inclusion might turn out to be beneficial because of the corresponding increase in the average neck size.⁴²

[36] K. Meier, T. Laino, A. Curioni, *J. Phys. Chem. C*, 2014, **118**, 6668.

[37] L. J. Miara, W. D. Richards, Y. E. Wang, *Chem. Mater.*, 2015, **27**, 4040.

[38] Y. Chen, E. Rangasamy, C. R. dela Cruz, *J. Mater. Chem. A*, 2015, **3**, 22868.

[39] G. Larraz, A. Orera, J. Sanz, *J. Mater. Chem. A*, 2015, **3**, 5683.

[40] M. Xu, M. S. Park, J. M. Lee, et al. *Phys. Rev. B*, 2012, **85**, 052301.

[41] V. Thangadurai, D. Pinzaru, S. Narayanan, *J phys. Chem. Let.*, 2015, **6**, 292.

[42] S Mukhopadhyay, T. Thompson, J. Sakamoto, *Chem. Mater.*, 2015, **27**, 3658.

③ Densification of the calcinations process

We fabricated an ultra-dense LLAZO ceramic disc by SPS, revealing that this material exhibited a primary grain size (10–100 μm , Figure 1a in manuscript) ten times that of the solid-phase-sintered product, sparse micro-pores, and a relative density of 99.2%. Even if it was thinned to 500 μm , the aqueous solution was completely isolated by the ultra-thin ceramic disc. A water droplet covered the surface of the LLAZO SSE and there was no significant change even after 360 s (Figure 1b in manuscript). These test results demonstrate the compactness of LLAZO solid-state electrolyte.

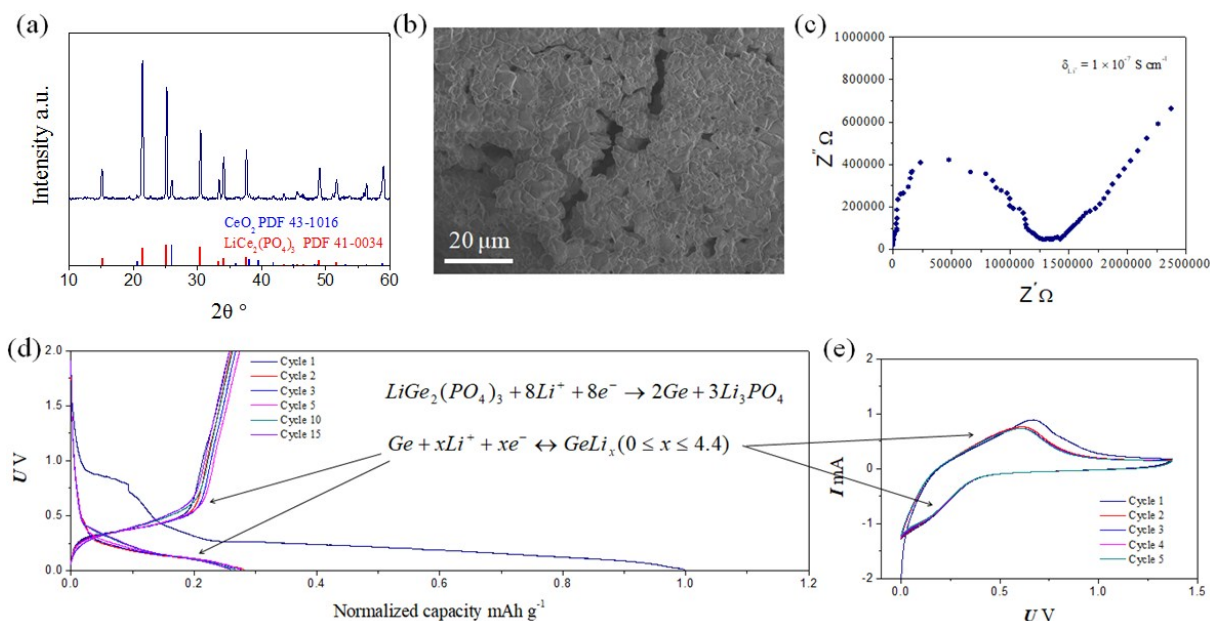


Figure S13. Characterization of physical properties of $\text{LiGe}_2(\text{PO}_4)_3$. (a) XRD; (b) SEM; (c) EIS; (d) charge-discharge curves and (e) CV.

$\text{LiGe}_2(\text{PO}_4)_3$ (LGP) was obtained by conventional solid-state method. The starting materials were Li_2CO_3 (99%, Aladdin), GeO_2 (99.9%, Aladdin), and $\text{NH}_4\text{H}_2\text{PO}_4$ (98%, Aladdin). Stoichiometric amounts of these chemicals were dispersed in deionized water and a 10% excess of Li_2CO_3 was added to compensate for Li volatilization during the high-temperature pellet preparation. The ball-milled mixture was evaporated at $120\text{ }^\circ\text{C}$ for 12 hours and then calcined to $400\text{ }^\circ\text{C}$ for 2 hours to synthesize the precursor powder. The powders were pressed into pellets and were then sintered at $1150\text{--}1250\text{ }^\circ\text{C}$ for 24 h with more of the LGP powder covering them in order to improve their crystallinity. XRD pattern of the LGP product matched that of NASICON structure (PDF 41-0034). A large number of micropores were observed at the cross section of the LGP pellet. The Li-ion conductivity was calculated to be $1 \times 10^{-7}\text{ S cm}^{-1}$ at 308 K derived from the intercept of the semicircle with the real axis. The charge-discharge curves of the Li/LGP half cell in the first 15 cycle between 0.001 V and 2.0 V were measured at the current density of 0.1 mA cm^{-2} . The half battery exhibited a reversible capacity of 150 mAh g^{-1} in the 2nd – 15th cycles, corresponding to the Li plating/stripping

reaction of GeO_2 . The peak corresponding to the reversible reaction was also observed on the CV curve. The test results show that the NASICON-type LGP is unstable to metallic lithium.

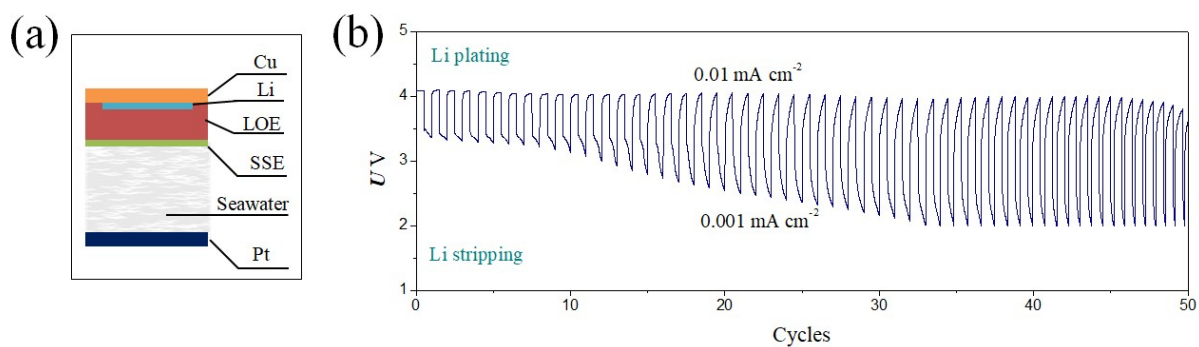


Figure S14. Li plating/stripping curves of the Li extraction device based on the $\text{LiGe}_2(\text{PO}_4)_3$ solid-state electrolyte. (a) Schematic diagram; (b) Li plating/stripping curves.

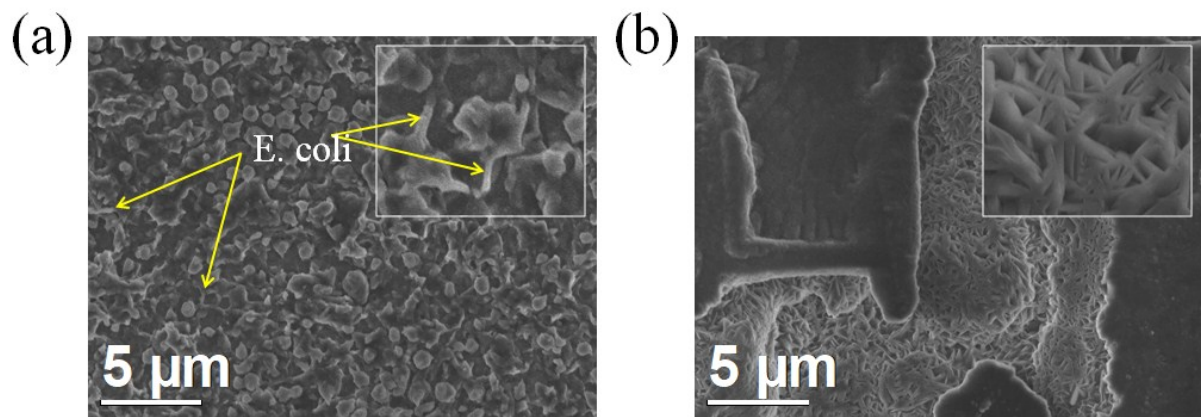


Figure 15. Characterization of the LLAZO biofouling. (a) SSE with *E. coli* attached; (b) SSE after seawater immersion.

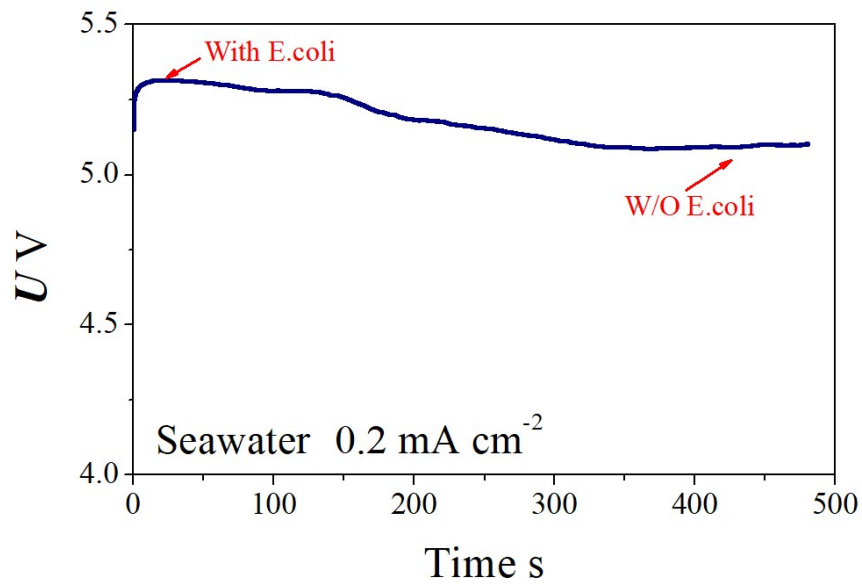


Figure 16. Constant current charge curve of in-situ cleaning battery with mixed gas.

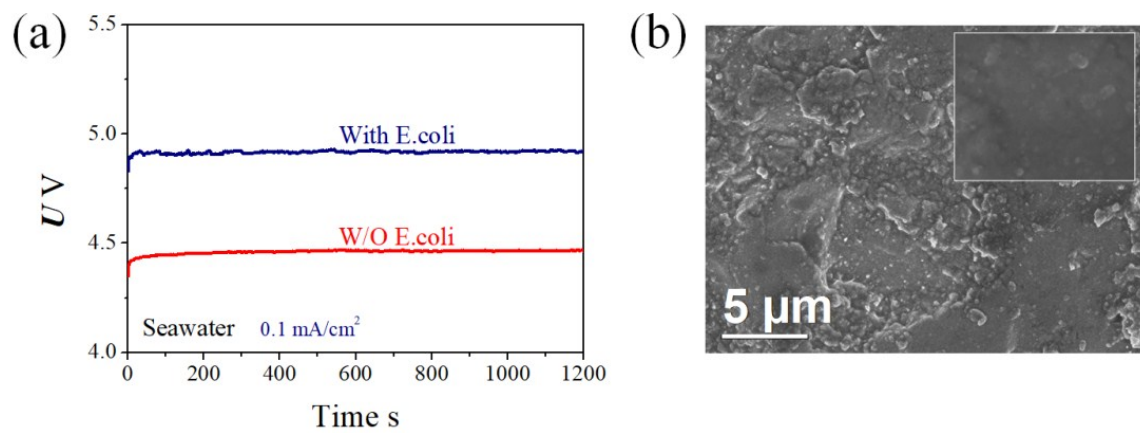


Figure 13. Characterization of the LLAZO anti-biofouling. (a) Current-time curves; (b) SEM image of the SSE after in-situ cleaning.